J. Nanostruct Chem. 2026; 16(2): 172-187

Journal of Nanostructure in Chemistry (JNSC)

https://doi.org/10.57647/jnsc.2026.1602.09

Research Article

Covalent Organic Frameworks-integrated Metal-Oxide-N-doped Catalysts: A Synergistic Approach to High Energy and Power Density

Rozhin Darabi[1,*], Anjana P.M[2], Tejraj M. Aminabhavi[2,3,4,*], Li Fu[5], Hassan Karimi-Maleh[6,7,*]

[1] *School of New Energy and Intelligent Connected Vehicle, University of Sanya, Hainan, 572022, China*
[2] *Center for Energy and Environment, School of Advanced Sciences, KLE Technological University, Hubballi, 580 031, India*
[3] *Korea University, Seoul 02841, Republic of Korea*
[4] *School of Engineering, University of Petroleum and Energy Studies (UPES), Dehradun, Uttarakhand, India 248 007*
[5] *Department of Material Science,* Hangzhou Dianzi University, *Hangzhou, China*
[6] *The Quzhou Affiliated Hospital of Wenzhou Medical University, Quzhou People's Hospital, Quzhou, 324000, China*
[7] *School of Chemistry, Damghan University, Damghan, 36716-45667, Iran*

* **Corresponding authors:** dr.darabirozhin@gmail.com, aminabhavit@kletech.ac.in, hassan@uestc.edu.cn

Article History:

Received:
10 November 2025

Revised:
02 January 2026

Accepted:
16 February 2026

Published in Issue:
30 April 2026

Abstract

Supercapacitors have played an important role in electrochemical energy storage. The performance characteristics of supercapacitor devices greatly depend not only on the electrode design but also on the core materials used in the electrode. In this study, we synthesised a new class of ternary materials that require simple methods of synthesis, involving a covalent organic framework (COF)-$NiCo_2O_4$-N-doped nanocomposite using a cost-effective hydrothermal route of synthesis. Composite electrode of COF/$NiCo_2O_4$-N-doped was developed that exhibited a high specific capacitance of 1,283.3 F g^{-1} at a discharge current density of 2 A g^{-1} when measured using a three-electrode setup. To show the potential of using COF/$NiCo_2O_4$-N-doped electroactive materials to create a practical and functional device, we fabricated an asymmetric supercapacitor (ASC) out of the COF/$NiCo_2O_4$-N-doped composite as the positrode and activated carbon (AC) as the negatrode in an electrolyte of 3 M KOH. The fabricated ASC device, COF/$NiCo_2O_4$-N-doped//AC exhibited impressive 34.59 Wh kg^{-1} and 1235.75 W kg^{-1} energy and power density ratings, respectively at a 2 A g^{-1} discharge current density, which maintained 90% rate of performance after 10,000 cycles of operation. Thus, the current study presents an efficient electrode material for deployment in energy storage devices of the future.

Keywords: COFs; Electrochemical stability; Pseudocapacitive; Supercapacitors; Transition metal oxide

Cite this article: Darabi R., Anjana P. M., Aminabhavi T. M., Fu L., Karimi-Maleh H. Covalent Organic Frameworks-integrated Metal-Oxide-N-doped Catalysts: A Synergistic Approach to High Energy and Power Density. *J Nanostruct Chem* **16**, 172-187 (2026).
https://doi.org/10.57647/jnsc.2026.1602.09

1. Introduction

Supercapacitors have become essential parts of many energy storage systems because of their extended cycle life, high power densities, and quick charge-discharge kinetics [1, 2]. However, supercapacitors still have a much lower energy density than lithium-ion batteries, but their energy density exceeds that of conventional capacitors by

many orders of magnitude [3, 4]. As a result, significant efforts have been expended to improve the functionality of supercapacitors through the development of a virtually limitless array of possible electrode materials. Electrode materials are generally be categorized based upon how they store energy viz., electric double-layer (EDL) capacitors and pseudo-capacitors [5, 6].

Recent and ongoing efforts to improve energy supply systems [7-16], there has been a lot of excitement surrounding covalent organic frameworks (COFs) due in part to their adjustable properties – such as excellent chemical stability, large surface area, and adjustable pore size [17, 18]. COFs formed from organic molecules that are covalently bonded together to form two-dimensional or three-dimensional crystalline porous materials [19]. Due to their modular design, which allows for the precise design of COF structure, they provide an excellent platform for the transport and storage of ions. Even though progress has been made in these areas, challenges still exist when it comes to improving the conductivity of COFs and scaling up their production. COFs containing redox-active metal cores such as Ni and Co demonstrated conductivities of 1.3×10^{-2} S cm^{-1}, which greatly improved their energy storage performance while maintaining long cycle stability [20, 21]. Metal oxides and other porous active materials can be developed by incorporating COFs.

Ternary transition metal oxides are becoming more popular for use as supercapacitor electrodes due to their greater conductivity and electrochemical activity compared to monomers of transition metal oxides [22-24]. Because of its high degree of durability, environmental friendliness, and significantly higher specific capacitance compared to those of the individual cobalt and nickel oxides, ternary $NiCo_2O_4$ was identified as a necessary electrode material for supercapacitors. Several nanostructured $NiCo_2O_4$ have been developed recently for use in high-performance supercapacitors [25, 26].

The low electrical conductivity of $NiCo_2O_4$, though still keeps it from being widely used in energy storage systems. Additionally, the durability of the electrode is significantly impacted by the volume contraction of $NiCo_2O_4$ throughout the electrochemical process. As a result, optimizing the microstructure of $NiCo_2O_4$-based electrode material is essential.

Integrating CNTs, graphene, and COFs is an effective technique that can prevent aggregation and enhance the electric conductivity of $NiCo_2O_4$-based electrode material by adapting to mechanical deformation during insertion and extraction [27-29]. COFs in particular provide exceptional thermal stability and excellent crystallinity, making them a unique template material for the fabrication of electroactive porous electrode materials. Another important tactic to increase the conductivity of $NiCo_2O_4$ electrode is doping with heteroatoms such as nitrogen (N) or phosphorus (P) [30, 31]. We developed an N-doped COF-modified $NiCo_2O_4$ ternary nanocomposite with a porous structure and a large surface area (provided by COF) as a matrix or framework for this purpose. The nanocomposite has decreased ionic volumes during swelling, providing rapid pathways for charge transport. The ternary $NiCo_2O_4$ includes nickel and cobalt ions, which experience redox reactions, thereby producing high specific capacitance.

The present study utilised a simple and economical hydrothermal method to synthesize ternary nanocomposite based on COFs combined with nitrogen-doped $NiCo_2O_4$ nanostructure for use in supercapacitors. Using COF/$NiCo_2O_4$-N-doped and activated carbon (AC) as the positive and negative electrodes, respectively an asymmetric supercapacitor (ASC) was constructed for practical deployment. The synthesized COF/$NiCo_2O_4$-doped material demonstrated a remarkable specific capacitance of 1283.3 F g^{-1} at 2 A g^{-1} in a three-electrode configuration, which showed its greater ability to incorporate as an electrode in commercial device assembly. The ASC device developed, which is represented as COF/$NiCo_2O_4$-doped//AC exhibited excellent energy and power densities of 34.59 Wh kg^{-1} and 1235.75 W kg^{-1}, respectively at 2 A g^{-1}, with 90% capacity retention over 10000 cycles. The outstanding performance of the ASC device is attributed to the exceptional pseudocapacitive properties of spinel $NiCo_2O_4$ nanostructure, the large active surface area from the porous COF template, and enhanced electronic conductivity due to N-doping.

2. Experimental

2.1. Synthesis of COF

The COF was fabricated through a Schiff-base condensation process involving benzene-1,3,5-tricarboxaldehyde (BTC-aldehyde) and melamine. Specifically, 21 mmol of BTC-aldehyde was dissolved in 25 mL of o-dichlorobenzene under stirring, followed by the addition of 21 mmol of melamine. The mixture was maintained at 150 °C for 48 h in a sealed vessel to facilitate imine linkage formation. After the reaction, the resulting was collected by centrifugation, washed with tetrahydrofuran (THF) and methanol to remove any unreacted residues, and dried at 80°C for 2 h to obtain the final COF product.

2.2. Synthesis of $NiCo_2O_4$-N-Doped

$NiCo_2O_4$ nanostructures were synthesized via hydrothermal method. Initially, 0.58 g of [$Co(NO_3)_2 \cdot 6H_2O$], 0.21 g of [$Ni(NO_3)_2 \cdot 6H_2O$], 0.74 g of ammonium fluoride (NH_4F), and 2.4 g of urea (CH_4N_2O)

10.57647/jnsc.2026.1602.09

were dissolved in 50 mL of deionized (DI) water under continuous magnetic stirring for 30 min at room temperature. The homogeneous solution was transferred into a Teflon-lined stainless-steel autoclave and heated at 120°C for 24 h. After naturally cooling to room temperature, the precipitate was separated by centrifugation, thoroughly washed with ethanol and deionized water, and then dried at 70°C. To introduce nitrogen doping, the as-prepared $NiCo_2O_4$ precursor was mixed with additional urea (as a nitrogen source) in DI water and stirred until a uniform dispersion was obtained. The mixture was dried at 120°C to form a solid precursor, which was subsequently calcined in air at 300°C for 3 h.

2.3. Synthesis COF/ $NiCo_2O_4$-N-Doped nanocomposites

The COF/$NiCo_2O_4$-N-doped nanocomposite was synthesized via hydrothermal method. First, 0.5 g of the synthesized COF was dispersed in 50 mL of ethanol and subjected to ultrasonic treatment for 30 min to form stable suspension. Then, 0.5 g of the previously prepared $NiCo_2O_4$-N-doped powder was added to the suspension, and the mixture was magnetically stirred for 1 h to ensure uniform dispersion. The resulting mixture was transferred to a Teflon-lined stainless-steel autoclave and heated at 120 °C for 8 h to facilitate the anchoring of $NiCo_2O_4$-N-doped particles onto the COF surface. Following the hydrothermal reaction, the composite was collected by centrifugation, washed multiple times with a 1:1 mixture of ethanol and deionized water to remove unbound residues, and then dried in a vacuum oven at 70°C for 10 h to obtain the final COF/$NiCo_2O_4$-N-doped nanocomposite.

2.4. Electrode fabrication for supercapacitor cell

Nickel foam (NF) was employed as the current collector for electrode fabrication. The active electrode material was prepared by blending COF/$NiCo_2O_4$-N-doped composite (85 wt) with carbon black (10 wt) as the conductive additive and polyvinylidene fluoride (PVDF, 5 wt%) as the binder. The mixture was then dispersed in n-methyl-2-pyrrolidone (NMP) to form a homogeneous slurry, which was uniformly coated onto the surface of pre-cleaned nickel foam and dried at 60°C to obtain the working electrode.

2.5. Assembling an asymmetric supercapacitor cell

The asymmetric supercapacitor cell was assembled using two distinct electrode materials; the COF/$NiCo_2O_4$-N-doped composite deposited onto nickel foam (NF) as the positive electrode, and activated carbon (AC) coated onto NF as the negative electrode. To prepare the negative electrode, AC and polyvinylidene fluoride (PVDF) were mixed at a mass ratio of 93:7 using a minimal amount of n-methyl-2-pyrrolidone (NMP) as the dispersing solvent. The resulting slurry was stirred vigorously for 2 h to ensure uniform dispersion, then applied onto NF substrate and dried at 60 °C overnight.

The ASC cell was assembled by stacking the positive and negative electrodes with a Whatman filter paper separator fully soaked in the electrolyte to ensure efficient ionic transport. The mass of AC electrode was carefully tadjusted based on charge-balance calculations to optimize the overall electrochemical performance of the ASC cell.

2.6. Examination of Materials

Thermoscientific Apreo 2 S and Oxford Ultim Max40 (SEM) and Thermoscientific Talos F200XG2 (TEM), Oxford Cypher S (AFM) instruments were used for morphological and elemental analysis of synthesized materials. Shimadzu XRD-6100 diffractometer with Cu-Kα radiation (λ = 1.54184 Å) was used for crystal structure investigation. Thermo ESCALAB 250Xi (XPS) was used for surface chemical composition and elemental states analysis of the synthesized materials. Nicolet Magna-550 (FTIR) was used for functional group analysis of the materials. Also, Micromeritics ASAP 2460 (BET) instrument was employed to determine specific surface area and pore size distribution of the catalyst.

2.7. Electrochemical experiments

Electrochemical tests were carried out using three-electrode system coupled with CHI 660E electrochemical workstation (Shanghai CH Instruments, China) in a 3M KOH alkaline electrolyte. where the nanocomposites-coated nickel foam served as the working electrode, a platinum plate, Ag/AgCl (3.0 M KCl) acted as the counter and reference electrodes, respectively. CV signals were recorded at various scan rates to investigation of the redox activity and capacitive behaviour of the systems. The GCD tests were recorded at different current densities, to calculation some important parameters of system such as specific capacitance (C, F g^{-1}), energy density (E, Wh kg^{-1}), and power density (P, W kg^{-1}), based on the following equations:

$$C = \frac{I\Delta t}{m\Delta V} \quad (1)$$

$$E = \frac{1}{2}CV^2 \quad (2)$$

$$P = \frac{E}{td} \quad (3)$$

where I is the discharge current (A), Δt is the discharge time (s), m is the mass of active material (g), and ΔV is the voltage window (V). In addition, the EIS measurements (frequency range of 0.01 Hz to 100 kHz and AC

10.57647/jnsc.2026.1602.09

perturbation of 5 mV) was applied to study of charge transfer resistance (R_{ct}) and relative factors using the Nyquist plots.

3. Results and discussions

3.1. Catalyst evaluation

Fig. 1(a–c) presents Fourier-transform infrared (FTIR) spectra of pristine COF, COF/$NiCo_2O_4$, and COF/$NiCo_2O_4$-N-doped composites, respectively. In all the samples containing $NiCo_2O_4$, characteristic absorption bands appear in the range of 523–688 cm^{-1}, attributed to the stretching vibrations of Ni–O and Co–O bonds at the octahedral sites of the spinel structure, confirming successful incorporation of the metal oxide phase [32, 33]. The pristine COF spectrum exhibits a strong absorption peak at ~1600–1639 cm^{-1} corresponding to C=N stretching vibration of the imine linkage formed via Schiff-base condensation between BTC-aldehyde and melamine, verifying the successful synthesis of the framework. Additional bands at 1495 cm^{-1} and 2217 cm^{-1} are assigned to C=C aromatic stretching and CH_2 vibrational modes, respectively, while the broad band around ~3507 cm^{-1} corresponds to O–H stretching, likely due to the adsorbed moisture or residual functional groups. Upon integration with $NiCo_2O_4$, the FTIR spectrum of COF/$NiCo_2O_4$ composite retains the key imine and aromatic signals, suggesting that COF's structural integrity is preserved. The appearance of metal–oxygen vibrational modes supports the formation of a hybrid organic–inorganic architecture. In the COF/$NiCo_2O_4$-N-doped sample, the peaks become broader and less intense, reflecting structural modifications and potential electronic interactions introduced due to nitrogen doping. Slight shifts and intensity changes in the C=N stretching region further indicate the chemical interactions between the doped $NiCo_2O_4$ network and the COF matrix, consistent with the formation of a conductive and electrochemically active nanocomposite.

Fig. 1d shows the XRD pattern of the synthesized COF. The diffraction profile exhibits a broad reflection centered around 25.6°, corresponding to the (002) plane associated with π–π stacking and the formation of imine-linked layers. Additional weak features in the low-angle region (10–12° and 18–20°) indicate short-range periodicity within the framework. These data collectively demonstrate that the COF structure is well-formed and preserved.

Fig. 1e presents XRD pattern of the COF/$NiCo_2O_4$-N-doped composite, showing the coexistence of organic and inorganic phases. The characteristic diffraction peaks at 2θ = 18.2°, 36.4°, 44.7°, 59.1°, and 65.3° correspond to the (111), (311), (400), (511), and (440) planes of cubic spinel $NiCo_2O_4$ (JCPDS No. 20-0781), confirming the successful incorporation of the metal oxide into the hybrid material. Additional weak peaks near 25 and 40 degrees confirm minor changes in the crystal lattices, which are probably due to nitrogen doping and may cause electronic interactions with the COF matrix. The presence of a broad peak at about 25.6 degrees corresponds to the (002) plane of the COF, which confirms the preservation of the COF structure within the composite.

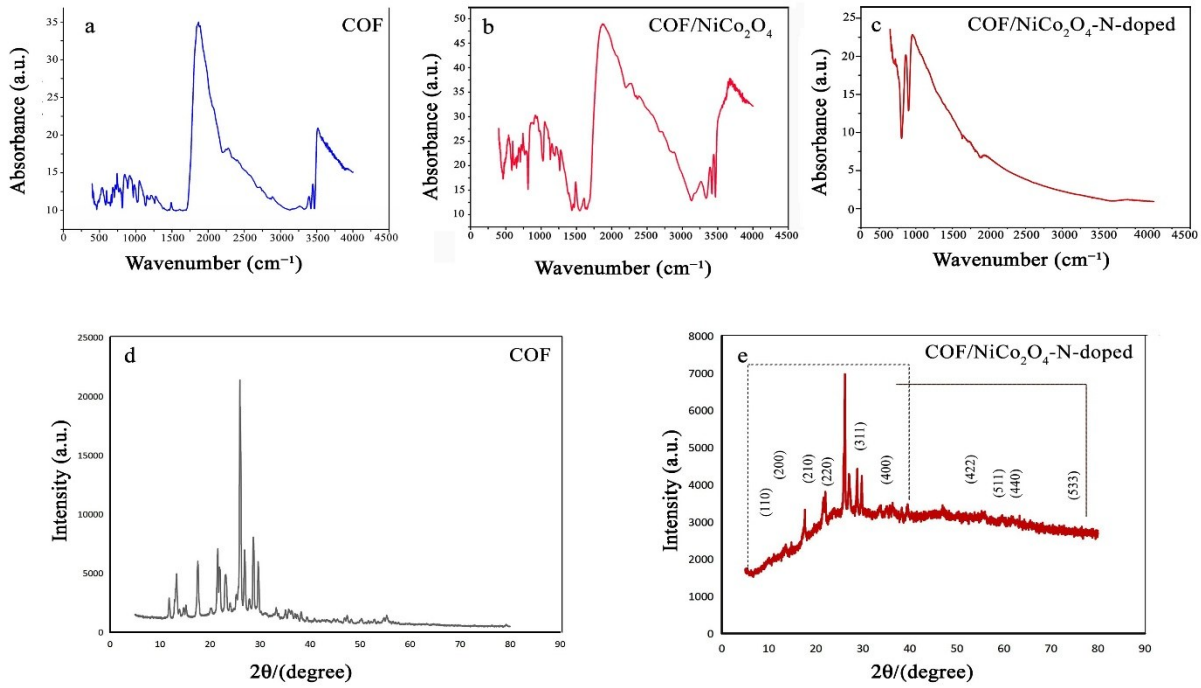

Figure 1. FTIR spectra of (a) pristine COF, (b) COF/$NiCo_2O_4$, and (c) COF/$NiCo_2O_4$-N-doped, and XRD patterns of (d) COF and (e) COF/$NiCo_2O_4$-N-doped

10.57647/jnsc.2026.1602.09

Small changes along with a slight broadening of the peaks in the peak presented after N doping confirming minor changes in the lattice and a decrease in crystallite size that are consistent with the formation of a hybrid nanocomposite. Fig. 2 displays SEM images of the nanohybrid and analyzes its morphological characteristics. The micrograph in Fig.2a shows agglomerated nanostructured particles with rough surfaces, which is a characteristic of the $NiCo_2O_4$-N doped compound. Fig. 2b well demonstrates the layered and planar morphology of the COF compound with well-defined planar structures, which are typical of imine-linked crystal frameworks. Fig. 2c to Fig. 2f provide a morphological study of the COF/$NiCo_2O_4$-N doped composite and evaluate their structure. The images confirm that the composite exhibits distinct structural features with its constituent components, namely COF and $NiCo_2O_4$. It can be observed that the $NiCo_2O_4$-N doped nanoparticles are uniformly deposited on the COF surfaces. These images were confirmed by elemental mapping and energy dispersive X-ray spectroscopy (EDX), which showed a homogeneous distribution of the constituent elements and confirmed the successful formation of a chemically uniform nanocomposite, as previously suggested by XRD results. Fig. 3 displays elemental distribution maps of COF/$NiCo_2O_4$-N-doped composite and EDX spectrum (a-g). In Fig. 3a, the composite morphology is highlighted through a color-overlay SEM image, showing the fibrous and interconnected surface structure.

Elemental mapping images (Fig. 3(b–f)) confirm uniform spatial distribution of the key elements within the nanocomposite including oxygen (O, b), chloride (Cl, c), cobalt (Co, d), carbon (C, e), and nickel (Ni, f). The consistent signal intensity across each element map supports the homogeneous integration of $NiCo_2O_4$ and nitrogen species throughout the COF matrix. EDX spectrum in Fig. 3g validates elemental composition, showing clear peaks for C, O, Co, and Ni confirming successful synthesis of the hybrid material. Nitrogen, due to its low atomic number, is not clearly observed in EDX. Minor signals from Si and Cl may originate from the substrate or precursor residues. These results corroborate the XRD and SEM findings, demonstrating the successful formation of a chemically uniform, nanostructured COF/$NiCo_2O_4$-N-doped composite with a compositionally balanced and electrochemically active surface.

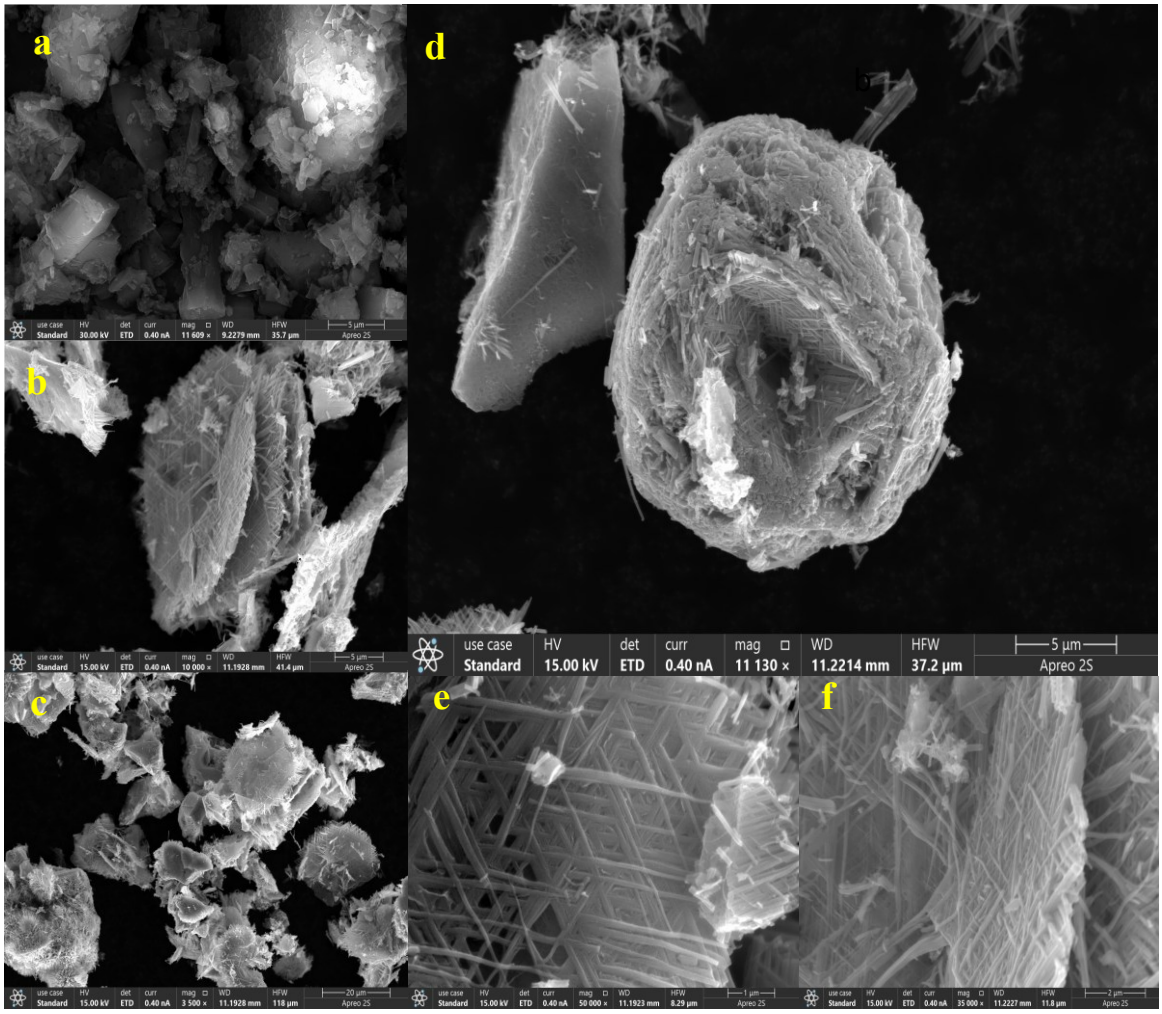

Figure 2. SEM images of (a) $NiCo_2O_4$-N-doped, (b) COF, (c to f) COF/$NiCo_2O_4$-N-doped

10.57647/jnsc.2026.1602.09

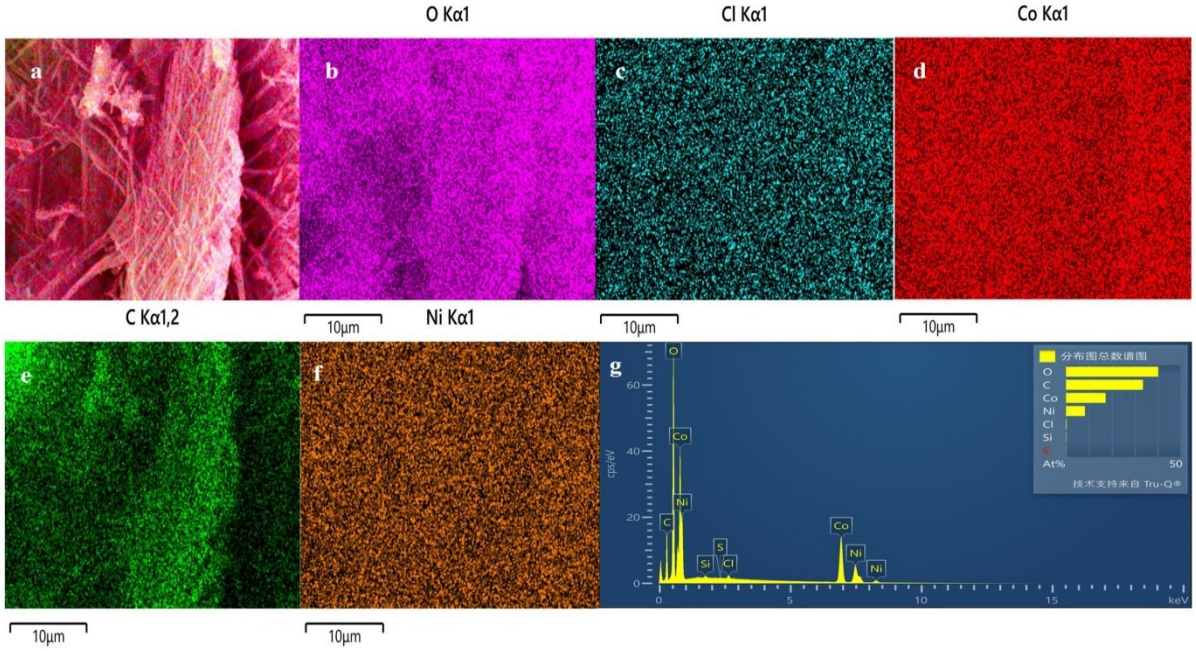

Figure 3. EDX mapping analysis of COF/$NiCo_2O_4$-N-doped

Fig. 4a–c shows the surface area and porosity characteristics of the catalyst, which were assessed through nitrogen adsorption–desorption isotherms at 77.3 K. The adsorption isotherm (Fig. 4a) exhibits a reversible Type IV behavior with a distinct hysteresis loop, which is indicative of the mesoporous structures. This behavior confirms the presence of capillary condensation, suggesting a well-developed pore network within the composite. BET surface area and Langmuir surface area were calculated to be 107.45 and 120.67 m2/g, respectively, confirming that the materials have high external surface accessibility. The BJH pore size distribution is shown in Fig. 4b and shows a relatively narrow distribution with a size of about 29.7 nm, confirming the mesoporous structure of the material. The pore volume of 0.034 ml/g indicates that the composite is suitable for electrochemical storage systems, where ion accessibility and diffusion pathways are very important. The results confirm the uniformity of the pore size, indicating a high level of structural order and crystallinity of the COF, which can be attributed to the regular lattice structure of the composite as well as its effective hybridization with $NiCo_2O_4$. Fig. 4d–g presents atomic force microscopy (AFM) images used for topographic investigations of surface morphology of the nanocomposite.

The AFM images in Fig. 4(d–g) show the measured surface of individual sections at 1 μm and 2 μm, with Adev [Ra] values of 4.312 nm and 44.536 nm for the roughness parameters, respectively. Figs. 4d and F44e confirm the surface with higher nanoscale domains, which can be a confirmation of the $NiCo_2O_4$-N clusters embedded in the COF layers. The 3D image in Fig. 4e also shows sharp vertical features, which are consistent with the fibrous and granular morphologies found for the synthetic hybrid. Meanwhile, the phase contrast and surface roughness maps (Figs. 4f and 4g) show nanoscale uniformity and depth variations throughout the film, which can support the system efficiency in terms of improved contact with the efficient charge-transfer electrolyte during supercapacitor operation. The XPS technique was used to investigate elemental composition and oxidation states in the COF/$NiCo_2O_4$-N doped nanocomposite (Fig. 5). The data in Fig. 5f confirmed the presence of carbon (C), nitrogen (N), oxygen (O), cobalt (Co), and nickel (Ni) elements, while confirming the successful incorporation of all components into the composite hybrid. Also, C1s, N1s, O1s, Co2p, and Ni2p spectra were recorded to evaluate the chemical bonding environments and valence states. In the C1s spectrum (Fig. 5a), the peaks located at ~284.6 eV, ~284.9 eV, and ~285.0 eV correspond to C-C/C=C, C-N, and C=O bonds, respectively, indicating the preserved chemical functionality of the COF skeleton and the incorporation of N-containing species. The N 1s spectrum (Fig. 5c) shows peaks at around 399.3 eV and 400.0 eV, corresponding to pyridinic/pyrrolic nitrogen and graphitic nitrogen, respectively. The Co 2p spectrum (Fig.5b) reveals two spin-orbit doublets and associated shake-up satellite peaks, consistent with the coexistence of Co^{2+} and Co^{3+} oxidation states. Peaks observed at ~780.2 eV (Co $2p_{3/2}$) and ~795.5 eV (Co $2p_{1/2}$) further support the formation of $NiCo_2O_4$ spinel phase. Similarly, Ni 2p spectrum (Fig. 5d) exhibits two well-defined spin-orbit doublets at ~855.5 eV (Ni $2p_{3/2}$) and ~873.2 eV (Ni $2p_{1/2}$), along with shake-up satellites, confirming the coexistence of Ni^{2+} and Ni^{3+} oxidation states and supporting the hybrid's redox-active nature.

10.57647/jnsc.2026.1602.09

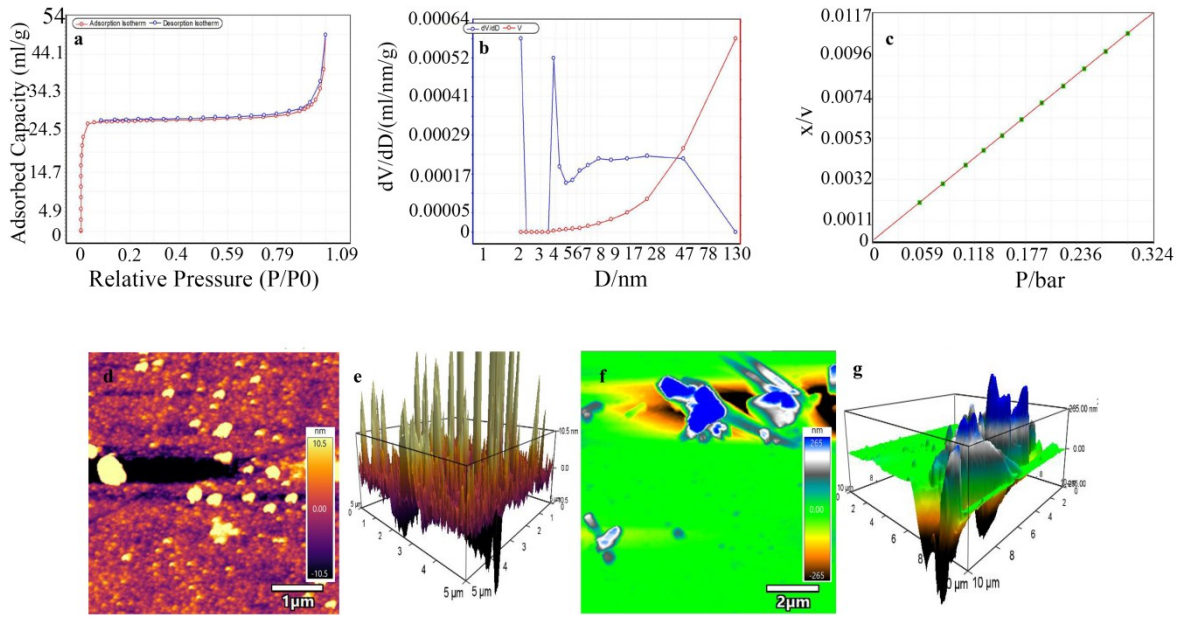

Figure 4 (a to c). Nitrogen adsorption/desorption isotherms and pore size distributions of the COF/$NiCo_2O_4$-N-doped and (d to g) AFM analysis of COF/$NiCo_2O_4$-N-doped

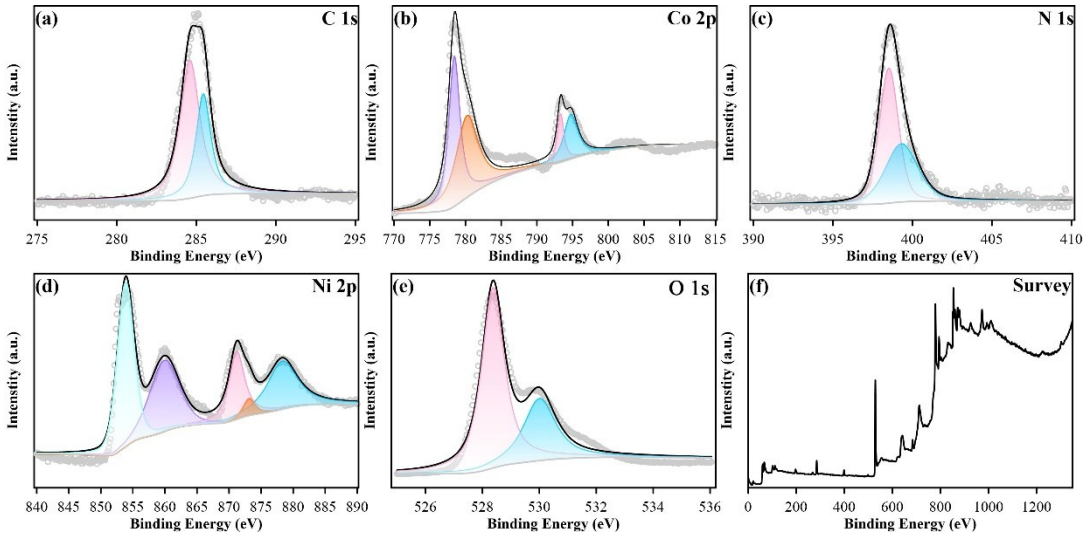

Figure 5. The high-resolution XPS spectra of COF/$NiCo_2O_4$-N-doped (a) C1s, (b) Co 2p, (c) N 1s, (d) Ni 2p, (e) O 2p and (f) full range XPS survey

The O 1s spectrum (Fig. 5e) can be deconvoluted into two principal peaks: the first, at ~528.5 eV, corresponds to metal–oxygen (M–O) bonds, while the second, at ~530.0 eV, is assigned to surface-adsorbed oxygen species or oxygen in under-coordinated environments. These features reflect the combination of lattice oxygen and surface-bound oxygen functionalities contributing to enhanced electrochemical reactivity.

These results validate the structure of the $NiCo_2O_4$ surface [34, 35]. The XPS results confirm the effective incorporation of N-doped carbon and $NiCo_2O_4$ into COF structure, highlighting the composite's potential for energy storage and catalytic applications. Fig. 6(a–g) shows TEM images of the doped COF/$NiCo_2O_4$-N nanocomposite, while Fig. 6(h) shows the selected area electron diffraction (SAED) pattern. TEM images clearly demonstrate the interconnected structure consisting of thin, wrinkled nanosheets and flower-like clusters that are characteristic of COFs. Fig. 6(a–e) shows the composition of one-dimensional $NiCo_2O_4$ nanostructures embedded as dark-contrast rods or wires within and across the layered COF matrix.

The high-resolution TEM images in Fig. 6f and Fig. 6g further confirm the crystalline nature of the embedded $NiCo_2O_4$ particles and the close contact between the organic and inorganic phases. The lattice fringes are clearly visible, indicating distinct crystal planes and strong interfacial integration between the components. The SAED pattern (Fig. 6h) shows concentric diffraction rings corresponding to specific lattice planes with the index (222), (400) and (440), which are characteristic of the spinel structure of $NiCo_2O_4$. These rings confirm polycrystalline nature of the composite and corroborate the XRD and XPS findings.

10.57647/jnsc.2026.1602.09

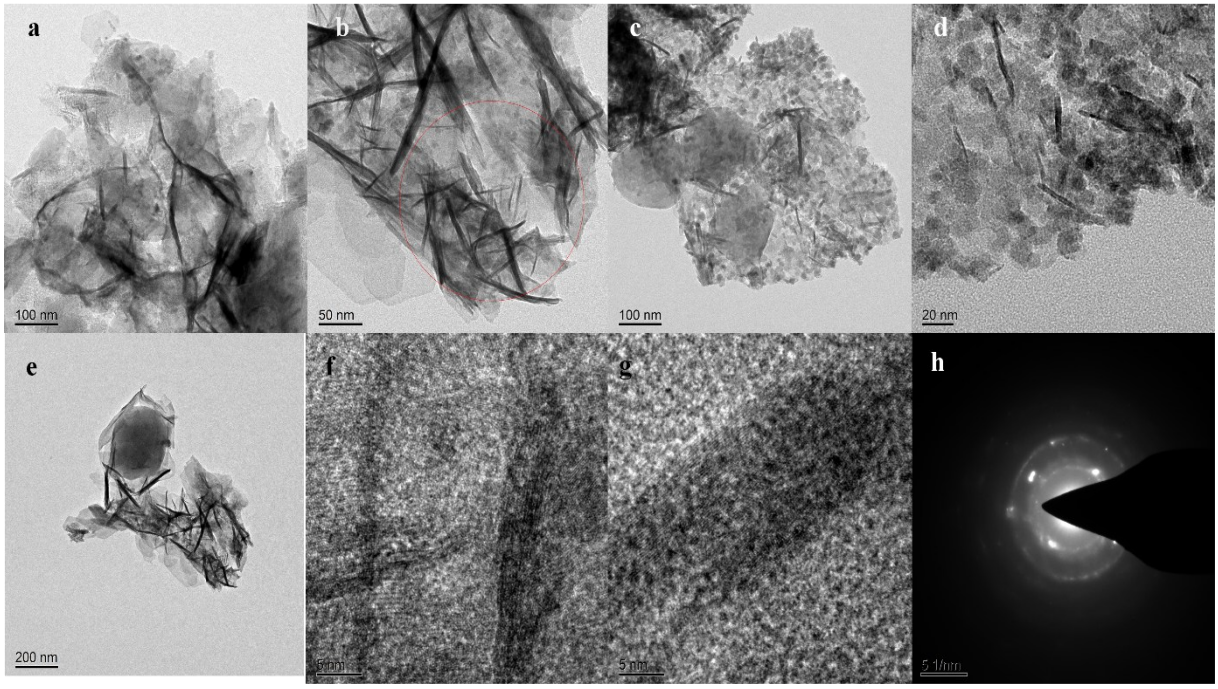

Figure 6 (a to g). TEM image of COF/$NiCo_2O_4$-N-doped and (h) SAED pattern of COF/$NiCo_2O_4$-N-doped

The results of BET analysis confirm favorable surface area and pore size distribution, which can promote rapid diffusion of ions into the system. SEM and TEM images (Figs. 2 and 6) reveal a highly interconnected structure, including thin and wrinkled nanosheets and well-dispersed $NiCo_2O_4$ nanostructures. High-resolution TEM and SAED confirm the crystalline nature and close contact between the COF and $NiCo_2O_4$ phases, which support efficient redox activity. XPS also identifies pyridinic, pyrrolic, and graphitic nitrogen species, along with Co^{2+}/Co^{3+} and Ni^{2+}/Ni^{3+} oxidation states, which collectively enhance the conductivity and provide active sites for Faradaic reactions. These structural and chemical properties synergistically contribute to the observed high specific capacity, excellent rate capability, and superior cyclic stability of the hybrid electrode.

As expected, the good electrochemical performance of COF/$NiCo_2O_4$-N doped nanocatalyst can be attributed to synergistic effect resulting from the close interaction between the COF matrix, $NiCo_2O_4$ nanoparticles and nitrogen doping. TEM, SEM and EIS images showed uniform dispersion and close contact between the organic and inorganic phases to some extent, which would facilitate efficient electron transfer in the electrochemical system and reduce the charge transfer resistance. Nitrogen doping introduces pyridinic, pyrrolic and graphitic nitrogen species, which provide additional electroactive sites for Faradaic reactions and enhance the electrical conductivity. The high surface area and porous structure of the COF ensure fast ion diffusion, while $NiCo_2O_4$ contributes to the active redox centers and overall promotes the improved quasi-capacitive behavior. This combination of structural, chemical features and electronic, supported the observed high specific capacitance, superior rate capability, and excellent cycling stability, clearly demonstrating the functional synergy among the components. Overall, the TEM and SAED results indicate a nanocomposite with a uniform dispersion, coherent structure and highly porous structure.

The results of BET analysis confirm favourable surface area and pore size distribution, which can promote rapid diffusion of ions into the system. SEM and TEM images (Figs. 2 and 6) reveal a highly interconnected structure, including thin and wrinkled nanosheets and well-dispersed $NiCo_2O_4$ nanostructures. High-resolution TEM and SAED confirm the crystalline nature and close contact between the COF and $NiCo_2O_4$ phases, which support efficient redox activity. XPS also identifies pyridinic, pyrrolic, and graphitic nitrogen species, along with Co^{2+}/Co^{3+} and Ni^{2+}/Ni^{3+} oxidation states, which collectively enhance the conductivity and provide active sites for Faradaic reactions. These structural and chemical properties synergistically contribute to the observed high specific capacity, excellent rate capability, and superior cyclic stability of the hybrid electrode. As expected, the good electrochemical performance of COF/$NiCo_2O_4$-N doped nanocatalyst can be attributed to synergistic effect resulting from the close interaction between the COF matrix, $NiCo_2O_4$ nanoparticles and nitrogen doping. TEM, SEM and EIS images showed uniform dispersion and close contact between the organic and inorganic phases to some extent, which would facilitate efficient electron transfer in the electrochemical system and reduce the charge transfer resistance. Nitrogen doping introduces pyridinic, pyrrolic and graphitic nitrogen species, which provide additional electroactive sites for Faradaic

reactions and enhance the electrical conductivity. The high surface area and porous structure of the COF ensure fast ion diffusion, while $NiCo_2O_4$ contributes to the active redox centers and overall promotes the improved quasi-capacitive behaviour. This combination of structural, chemical features and electronic, supported the observed high specific capacitance, superior rate capability, and excellent cycling stability, clearly demonstrating the functional synergy among the components.

3.2. Electrochemical investigations of electrodes

Figure 7 shows the CV curves of the synthesized electrode materials, obtained at scan rates ranging from 5 to 100 mV s^{-1} in a three-electrode configuration, with 3.0 M KOH as the electrolyte, over a potential range of 0.0 to 0.6 V. Fig. 7 (a–d) correspond to different electrode compositions or structural variations of COF/$NiCo_2O_4$-N-doped nanocomposite. All the CV curves exhibit quasi-rectangular and redox-active profiles, indicating the coexistence of both electric double-layer capacitance (EDLC) and Faradaic pseudocapacitance mechanisms. The presence of distinct redox peaks in each sample confirms the reversible redox behavior of the Ni^{2+}/Ni^{3+} and Co^{2+}/Co^{3+} couples, typical of transition metal oxides in alkaline media. The redox peaks observed in the CV curves of the COF/$NiCo_2O_4$-N-doped/NF electrode correspond specifically to the Ni^{2+}/Ni^{3+} and Co^{2+}/Co^{3+} redox transitions, confirming the pseudocapacitive behavior of the material. As the scan rate increases, CV curves maintain their shape without significant distortion, highlighting good rate capability and fast electron/ion transport within the electrode structure. The increase in current with increasing scan rate well confirms the improvement and acceleration of the redox kinetics of the system and the efficient access of ions into the porous framework. It is noteworthy that wider current coverages observed in some panels (especially Fig. 7b and Fig. 7d) indicate a higher capacitive contribution, which is probably due to the surface optimization and enhanced electrochemical interactions between the COF matrix and the N-doped $NiCo_2O_4$ component. These observations can be considered as good evidence for the high electrochemical activity and stability of the hybrid electrodes and suggest it as a suitable system in efficient supercapacitor applications. Fig. 8(a) shows cyclic voltammetry (CV) responses of four separate electrodes, including COF/NF, $NiCo_2O_4$/NF, COF/$NiCo_2O_4$ and COF/$NiCo_2O_4$-N-doped/NF, recorded at a scan rate of 50 mV/s in 3.0 M KOH electrolyte, are presented and compared. The comparison of these four data shows that the COF/$NiCo_2O_4$-N-doped/NF electrode has the highest peak current response and the largest integrated CV area, confirming its more favorable charge storage performance than the other electrodes.

This improvement in efficiency can be attributed to the synergistic interaction between the redox-active $NiCo_2O_4$ nanoparticles, the high surface area and porosity of the COF matrix, and the improved conductivity due to nitrogen doping.

The CV curve of the COF/N-doped $NiCo_2O_4$/NF electrode shows well-defined redox peaks centered at approximately 0.404 V (oxidation) and 0.206 V (reduction), indicating quasi-reversible Faradaic reactions associated with the Co^{2+}/Co^{3+} and Ni^{2+}/Ni^{3+} redox couples, confirming the quasi-capacitive nature of the catalyst. These findings validate the efficient integration of the COF, $NiCo_2O_4$, and nitrogen-doped components, which collectively contribute to enhanced electron transport, accessible ion pathways, and overall electrochemical performance, making this composite electrode a strong contender for advanced supercapacitor applications.

Fig. 8b presents the GCD profiles of four electrodes including COF/NF, $NiCo_2O_4$/NF, COF/$NiCo_2O_4$/NF, and COF/$NiCo_2O_4$-N-doped/NF recorded at a current density of 2 A g^{-1} within a potential window of 0.00–0.60 V. The discharge curves reveal a characteristic non-linear profile, typical of pseudocapacitive materials undergoing Faradaic reactions. Among the electrodes, COF/$NiCo_2O_4$-N-doped/NF sample exhibits the longest discharge duration, indicative of its superior charge storage capacity. The calculated specific capacitance values for the COF/$NiCo_2O_4$-N-doped/NF, COF/$NiCo_2O_4$/NF, $NiCo_2O_4$/NF, and COF/NF electrodes were 1283.3, 923.38, 550.0, and 316.66 F g^{-1}, respectively at 2 A g^{-1} current density. The enhanced performance of the ternary hybrid electrode is attributed to its synergistic architecture, which combines the electrical conductivity and redox activity of $NiCo_2O_4$ with the high surface area and ion diffusion channels provided by the COF, along with improved electronic transport pathways from nitrogen doping.

This architecture promotes rapid ion exchange at the electrode–electrolyte interface, thereby contributing to its outstanding electrochemical behavior. Figs. 8c and 8d illustrate the GCD profiles of COF/$NiCo_2O_4$-N-doped/NF electrode at varying current densities ranging from 2.0 to 9.0 A g^{-1}. The composite maintains a nearly symmetrical charge–discharge profile, demonstrating excellent reversibility and rate capability. The electrochemical performance metrics calculated from GCD data obtained in a three-electrode electrochemical cell configuration are tabulated in Table 1. The specific capacitance values decline with increasing current density—from 1283.3 F g^{-1} at 2 A g^{-1} to 225 F g^{-1} at 9 A g^{-1}—a common behavior due to reduced electrolyte ion accessibility at higher current rates. The results of this electrode have shown good energy and power characteristics at the measured current densities.

10.57647/jnsc.2026.1602.09

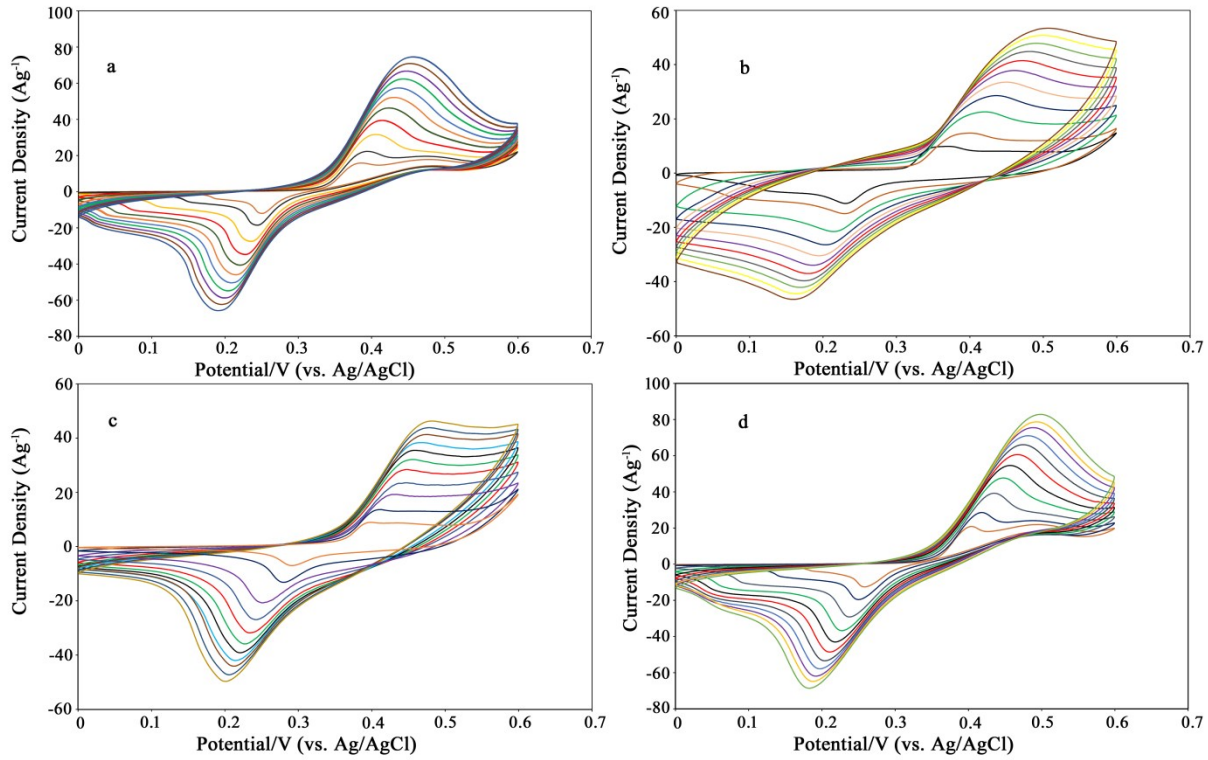

Figure 7(a to d). CV curves of as-prepared samples at different potential scan rates of 5, 10, 20, 30, 40, 50, 60, 70, 80, 90, and 100 mV s^{-1} in 3.0 M KOH electrolyte in a 3-electrode electrochemical cell

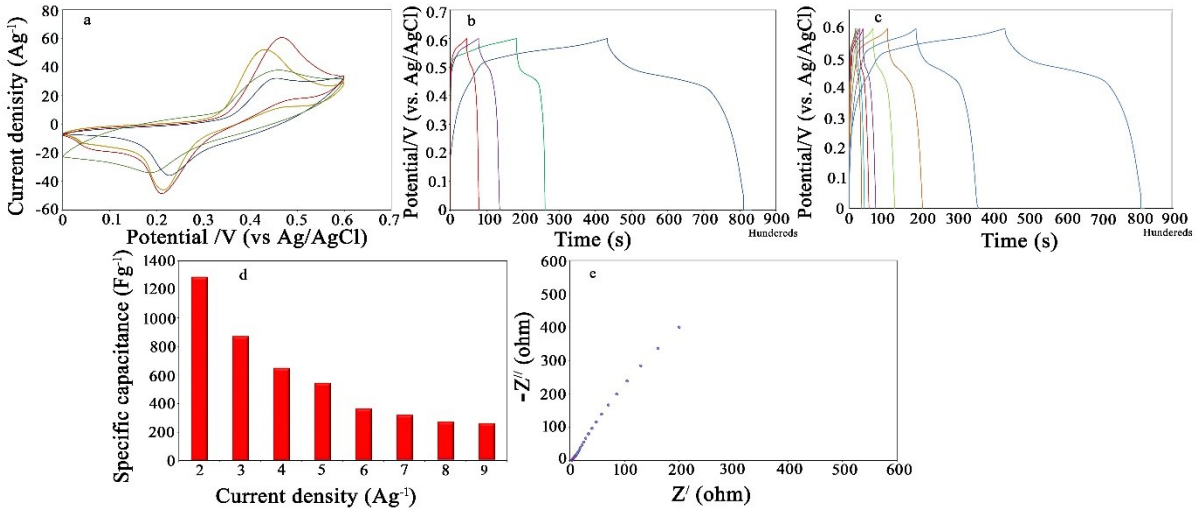

Figure 8. (a) CV and (b) GCD of different components from a to d, as: COF/NF, $NiCo_2O_4$/NF, COF/$NiCo_2O_4$, and COF/$NiCo_2O_4$-N-Doped at scan rate 50 mV.s^{-1} and current density of 2 A.g^{-1}, respectively. (c) GCD of COF/$NiCo_2O_4$-N-Doped at different current densities at 2, 3, 4, 5, 6, 7, 8, and 9 A.g^{-1} (a to h), (d) results of specific capacitance obtained from the GCD curves in different current densties , and (e) EIS diagrams of COF/$NiCo_2O_4$-N-Doped in 3 electrode system

These results confirm the ability of the COF/$NiCo_2O_4$-N doped nanocomposite as a catalyst in energy storage systems and could be an interesting and widely used proposal for next-generation supercapacitor devices.

Fig. 8e shows the Nyquist plot derived from electrochemical impedance spectroscopy for the COF/$NiCo_2O_4$-N-doped/NF electrode, and the results were used to investigate the charge transport in the system as well as capacitive behavior of the hybrid material. The presence of a small semicircle in the high-frequency region corresponds to a charge transfer resistance (Rct) of 67 Ω at the electrode–electrolyte interface. This value reflects the interfacial charge-transfer kinetics of the system. Although R_{ct} is not negligible, the integrated porous architecture and nitrogen doping contribute to improved ion diffusion and electron transport, which is consistent with the observed high specific capacitance. The low electrolyte resistance (Rs = 1.8 Ω) and minimal Rct confirm the formation of a conductive and integrated nanostructure that facilitates fast charge transfer, efficient

10.57647/jnsc.2026.1602.09

access to the electrolyte, and superior electrochemical performance. All these results can be attributed to the unique properties of the catalyst such as the porous COF architecture, redox-active $NiCo_2O_4$ nanoparticles, and enhanced conductivity due to nitrogen doping. The results of impedance studies confirm high specific capacitance values as well as excellent rate performance of COF/$NiCo_2O_4$-N-doped/NF electrode. However, it should be noted that the inverse relationship between specific capacitance and current density is shown in Fig. 8d. At higher current densities, the capacitance gradually decreases due to the diffusion-controlled charge storage mechanisms. With increasing current, the time for ions to diffuse into the deeper layers of the porous electrode structure decreases, which leads to less access to the electroactive sites and reduces the overall capacitance and energy storage efficiency. Accordingly, striking a balance between high power delivery and ion accessibility is very important and essential in the design of new electrodes. The hybrid nanocatalyst designed in this research work successfully solves this problem and offers a combination of low internal resistance, fast ion/electron transport, and strong quasi-capacitive response.

Table 1. Electrochemical performance characteristics of all electrode materials in 3.0 M KOH electrolyte in a three-electrode cell configuration at various current density values

Sample ID	Current Density ($A.g^{-1}$)	Specific Capacitance ($F.\ g^{-1}$)	E ($W.h.kg^{-1}$)	P ($W.\ kg^{-1}$)
COF/NF	2	316.66	15.83	608.84
	3	300.00	15.00	937.50
	4	206.66	10.33	1291.00
	5	204.00	10.00	1470.00
	6	190.00	9.50	1826.9
	7	186.66	9.33	2120.4
	8	180.00	9.00	2432.4
	9	165.00	8.25	2750.0
$NiCo_2O_4$/NF	2	550.00	27.50	500.00
	3	373.33	18.66	622.00
	4	290.00	14.50	906.25
	5	266.66	13.33	1211.8
	6	116.66	11.60	1315.2
	7	100.00	9.70	1616.0
	8	98.00	7.35	2227.2
	9	90.00	4.50	2025.0
COF/$NiCo_2O_4$	2	923.38	46.16	607.33
	3	820.0	41.0	911.11
	4	546.66	27.33	1203.9
	5	366.66	18.33	1502.45
	6	325.90	16.28	1629.0
	7	291.66	14.58	2082.85
	8	106.66	5.33	2225.0
	9	95.50	4.51	2652.9
COF/$NiCo_2O_4$-N-doped/NF	2	1283.3	64.15	641.50
	3	870.00	43.5	1087.5
	4	653.33	32.66	1633.0
	5	500.00	25.00	1562.0
	6	350.00	17.50	2250.0
	7	315.00	15.75	2250.0
	8	233.33	11.66	2332.0
	9	225.00	11.25	2812.5

10.57647/jnsc.2026.1602.09

The displayed results confirm proper performance of the nanocatalyst in the electron transfer process and on the other hand, the electrode performance showed improvement of conductivity and ion transport properties of the samples during electrochemical process. The research findings show the relationship between the values of specific capacitance and different current densities used. The observed decrease in specific capacitance with increasing current density confirms the systems that behave by a mechanism controlled by electrochemical capacitance diffusion. This indicates that with increasing charging rate, due to increasing current density, the specific capacitance decreases, as a result of which ions are prevented from transferring to the inner layers of the active material, thus affecting the overall energy storage capacity.

3.3. Evaluation of electrochemical performance of asymmetric supercapacitor cells

Considering the obtained capacitance as well as electrical conductivity of the COF/$NiCo_2O_4$-N doped electrode, an asymmetric supercapacitor (ASC) cell was designed with NF/COF/$NiCo_2O_4$-N doped as the positive electrode and activated carbon (AC/NF) as the negative electrode. Fig. 9 shows the CV curves in the operating range of 0.0 to 1.2 V for NF/COF/$NiCo_2O_4$-N//AC/NF doped asymmetric supercapacitor cell.

The NF/COF/$NiCo_2O_4$-N doped electrode exhibits a wide electrochemical stability range, with well-defined redox peaks extending up to about 0.6 V (vs. Ag/AgCl), indicating stable faradaic activity and a stable quasicapacitive mechanism. In contrast, the AC/NF electrode operates in a narrower potential range and exhibits typical electric double layer behavior without significant oxidation-reduction contributions. The resulting results enable the system to achieve a total cell voltage of 1.2 V without experiencing electrolysis or degradation. The quasi-rectangular CV shape of the hybrid electrode, even at higher scan rates, further confirms its electrochemical robustness, minimal polarization, and high reversibility.

The extended voltage range is not only thermodynamically permissible, but also practically viable, ensuring the optimal utilization of the hybrid electrode's redox capacity for enhanced energy storage performance. Fig. 9a displays the CV profiles of ASC device at various scan rates ranging from 10 to 140 mV s^{-1}. The CV curves retain a quasi-rectangular and redox-active shape even at high scan rates, suggesting excellent capacitive behavior and high-rate stability.The data reflect rapid electron/ion transport and stable pseudocapacitive characteristics within the composite structure. Galvanostatic charge–discharge of ASC cell curves at current densities from 2.0 to 8.0 A g^{-1} are presented in Fig. 9b, showing symmetric charge–discharge. The gradual decline in capacitance with increasing current density is typical of diffusion-limited ion transport under high-rate conditions but still indicates strong electrochemical resilience. The energy and power densities were calculated from the GCD profiles, revealing the outstanding performance.

The device achieved an energy density of 34.59 Wh kg^{-1} at a power density of 1235.75 W kg^{-1}, and retained 14.66 Wh kg^{-1} even at 4886.6 W kg^{-1}, clearly outperforming many conventional supercapacitors and approaching battery-level energy delivery in high-power conditions. These results validate the hybrid material's ability to bridge the gap between high energy and high-power demands.

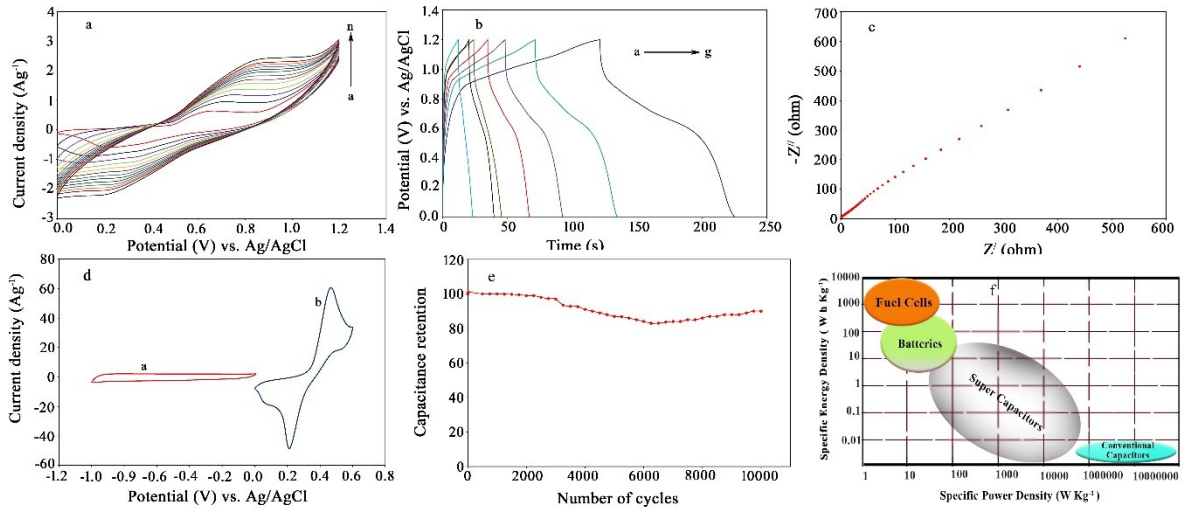

Figure 9. Electrochemical characteristics of the prepared asymmetric supercapacitor NF/ COF/$NiCo_2O_4$-N-doped//AC/NF: (a) CV curves of ASC cell at various potential scan rates of 10, 20, 30, 40, 50, 60, 60, 70, 80, 90, 100, 110, 120, 130 and 140 $mV.s^{-1}$ (a to n), (b) GCD curves of ASC at different current densities 2.0 to 9.0 to A. g^{-1}. (c) The Nyquist plot of the NF/COF/$NiCo_2O_4$-N-doped//AC/NF ASC cell (d) The CV voltammograms of (line a) NF/AC and (line b) NF/COF/$NiCo_2O_4$-N-doped electrodes in 3.0 M KOH at a potential scan rate of 50 mVs^{-1} in a 3-electrode electrochemical cell configuration (e) cycle performances at a sweeping scan rate 50 mV s^{-1}, (f) Ragone plots of ASC

10.57647/jnsc.2026.1602.09

Table 2. Comparative study of NF/COF/$NiCo_2O_4$-N-doped//AC/NF asymmetric supercapacitor cell with literature

Electrode material	Voltage window	Specific capacitance(F g^{-1})	Energy density (W h k g^{-1})	Cyclic stability	Ref.
N–C/$NiCo_2O_4$//AC	0 to 1.6 V (3 M KOH)	186.88 F g^{-1} at 1 A g^{-1}	66.44 W h kg^{-1} at 800 W kg^{-1}	93.66% (1000 cycles)	[37]
$NiCo_2O_4$/ZnO-CuO/NF//ASC	0 to 1.6 V (3 M KOH)	3614.8 F g^{-1} at 2 A g^{-1}	75.3 Wh kg^{-1} at 1549.2 W kg^{-1}	95% (40000 cycles)	[39]
$NiCo_2O_4$//Na_2SO_4/PAA// PCS	0 to 2.4 V	120 F g^{-1} at 1 A g^{-1}	104 Wh kg^{-1} at 10368 W kg^{-1}	79.4% (10000 cycles)	[40]
$NiCo_2O_4$//WSs-2	0 to 1.7 V (2 M KOH)	50.6 F g^{-1} at 1 A g^{-1}	21 Wh kg^{-1} at 424.5 W kg^{-1}	99.3% (5000 cycles)	[41]
NF/COF/$NiCo_2O_4$-N-doped//AC/NF	0 to 1.2 V (3 M KOH)	172.96 F g^{-1} at 2 A g^{-1}	34.59 Wh kg^{-1} at 1235.75 W kg^{-1}	90% (10000 cycles)	Present Work

The performance metrics of NF/COF/$NiCo_2O_4$-N-doped//AC/NF ASC cell show in Table S1 (Suplementary information data). Fig. 9c shows the Nyquist plot of the ASC cell. Although an increase in impedance is observed compared to the three-electrode configuration, the plot still demonstrates a relatively small semicircle at high frequency and a steep linear portion at low frequency, indicating low charge transfer resistance and effective ion diffusion. Fig. 9d illustrates the electrochemical properties of NF/AC and NF/COF/$NiCo_2O_4$-N-doped//AC/NF at a scan rate of 50 mVs^{-1}. Fig. 9e show the cyclability of the NF/COF/$NiCo_2O_4$-N-doped//AC/NF asymmetric supercapacitor cell, evaluated over 10,000 charge–discharge cycles at a continuous CV analysis at scan rate 50 mV s^{-1}. As observed, the designed system retains 90% of its initial specific capacity after long cycles, indicating its highly reversible redox reactions and excellent stability.

This exceptional cycle life is attributed to the stable integration of COF and $NiCo_2O_4$ nanostructures, which maintain mechanical integrity and conductive pathways throughout prolonged electrochemical stress. These results confirm the suitability of the composite electrode for long-term, high-performance energy storage applications. Fig. 9f presents the Ragone plot, which maps the relationship between specific energy (Wh kg^{-1}) and specific power (W kg^{-1}) of the NF/COF/$NiCo_2O_4$-N-doped//AC/NF ASC cell.

The electrochemical performance of the ASC device is comparable to some previously reported studies. For instance, Yuvaraja et al. [36], developed a $NiCo_2O_4$/carbon composite-based ASC device with an energy density of 20.3 Wh kg^{-1} and a power density of 406 W kg^{-1}. Zhou et al. [37] reported an N–C/$NiCo_2O_4$//AC device with a volumetric energy density of 66.44 mWh cm^{-3}. Mulik et al. [38] synthesized $NiCo_2O_4$/porous carbon from a bimetallic–organic framework and fabricated two asymmetric devices using $NiCo_2O_4$/PC as the cathode, and either activated carbon (AC) or polyaniline (PANI) as the anode.

Bhatti et al.[39] developed an ASC using $NiCo_2O_4$/ZnO-CuO/NF as the anode and activated carbon as the cathode, which demonstrated a power density of 1549.2 W kg^{-1} and an energy density of 75.3 Wh kg^{-1} at 2 A g^{-1}. The NF/COF/$NiCo_2O_4$-N-doped//AC/NF ASC device developed in this study exhibited an energy density of 34.59 Wh kg^{-1} and a power density of 1235.75 W kg^{-1}. These results highlight the material's ability to deliver moderate energy and high power, consistent with the synergistic combination of the pseudocapacitive COF/$NiCo_2O_4$-N-doped electrode and the EDLC-type AC electrode.

It seems that this device has the necessary capabilities and potential for use in energy storage systems such as hybrid electric vehicles and portable electronics.

4. Conclusions

In this study, ternary COF/$NiCo_2O_4$-N-doped nanocomposites were synthesized using a simple and inexpensive method; the synthesized material showed high potential for use in asymmetric supercapacitor applications.

The synthesized catalyst in the hybrid electrode structure exhibited suitable electrochemical properties for use as an asymmetric supercapacitor, including a high specific capacitance of 1283.3 F g^{-1} at 2 A g^{-1}, excellent rate capability (225 F g^{-1} at 9 A g^{-1}), and outstanding cycling stability, retaining 90% of its initial capacity over 10,000 cycles. The superior performance of the COF/$NiCo_2O_4$-N-doped/NF electrode in the energy storage system can be attributed to large specific surface area of the material, hierarchical porosity, and the synergistic effect between COF, $NiCo_2O_4$ spinel oxide, and nitrogen doping, which can create unique properties.

This work introduces a novel COF-based hybrid electrode architecture that effectively combines the advantages of conductive frameworks and pseudocapacitive metal oxides.

10.57647/jnsc.2026.1602.09

Competing Interests

There is no conflict of interest in this study

Declaration of generative AI

Authours used ChatGPT to improve the readability and language of the manuscript

Research Funding

This work was supported by the Hassan Research Initiation Fund Grant Number KYQD2024-046 and Theoretical and Experimental Development of an MXene/GoldAmplified Electrochemical Biosensor for Monitoring Lung Cancer Drugs: Adagrasib and Afatinib Dimaleate Grant Number 2025K064, The Quzhou Affiliated Hospital of Wenzhou Medical Universitv

References

[1] Zhang, Z., Xu, X., Xing, X., Tang, X., Zhang, X., Chen, J., Xu, Y., Jiang, H., Exquisitely functionalized porphyrin-COF self-supporting nanofilm for high-performance in-plane micro-supercapacitor. *Appl Surf Sci* **680**, 161327 (2025).

[2] Shanavaz, H., Alharethy, F., Jeon, B.H., Exploring the potential of metal tailored imine based covalent organic framework for asymmetric supercapacitor applications. *J Mol Struct* **1321**, 139983 (2025).

[3] Devendran, A., Nagai, A., Covalent Organic Framework-Derived Highly Defective Carbon-Integrated Polymer Composite Electrode for Supercapacitor Applications. *ACS Appl Energy Mater* **8**, 2597–2611 (2025).

[4] Aribou, Z., Mzioud, K., Ouakki, M., Ferraa, N., Bakkali, S., Touhami, M.E., Recent Advances in Supercapacitor Materials: A Review on Performance Enhancement, Flexibility, and Scalability for Next-Generation Energy Storage. *Advancements and Innovations in Electrochemical Conversion and Energy Storage*. (2026) 163-236.

[5] R. Darabi, M. Shabani-Nooshabadi, ZIF-8/Co-C3N4-GNR/MXene nanocomposites: A novel electrode material with excellent electrochemical properties for supercapacitors, *Alex Eng J* **129** (2025) 803-810.

[6] Darabi, R., Zare, N., Karimi-Maleh, H., Karimi, F. Novel ternary nanocomposites as a powerful catalyst for high-performance all-solid-state asymmetric supercapacitors. *Adv Compos Hybrid Mater* **7**, 184 (2024).

[7] Anakha, D., Nithyadas, K., Vyshnavi, T., Ananthkumar, M., Menon, P.R., Yamuna, R., Fabrication of CuO-βCD/Co-Al LDH nanocomposite for supercapacitor applications. *Carbon Lett* **35**, 2791-2807 (2025).

[8] Oladele, I., Adelani, S., Taiwo, A., Akinbamiyorin, I., Olanrewaju, O., Orisawayi, A., Polymer-based nanocomposites for supercapacitor applications: a review on principles, production and products. *RSC Adv* **15**, 7509-7534 (2025).

[9] Shariq, M., Alshehri, K., Bouzgarrou, S.M., Ali, S.K., Alqurashi, Y., Hassan, K., Azooz, R., Progress in development of MXene-based nanocomposites for supercapacitor application-A review. *FlatChem* **44**, 100609 (2024).

[10] Sharma, S., Chand, P., Supercapacitor and electrochemical techniques: A brief review. *Results Chem* **5**, 100885 (2023).

[11] Kumar, N., Kim, S.B., Lee, S.Y., Park, S.J., Recent advanced supercapacitor: a review of storage mechanisms, electrode materials, modification, and perspectives. *Nanomaterials* **12**, 3708 (2022).

[12] Attia, S.Y., Mohamed, S.G., Barakat, Y.F., Hassan, H.H., Zoubi, W.A., Supercapacitor electrode materials: addressing challenges in mechanism and charge storage. *Rev Inorg Chem* **42**, 53-88 (2022).

[13] Forouzandeh, P., Kumaravel, V., Pillai, S.C., Electrode materials for supercapacitors: a review of recent advances. *Catalysts* **10**, 969 (2020).

[14] He, Y., Liu, X., He, K., Kamyab, H., Gnanasekaran, L., Anjana, P.M., Aminabhavi, T.M., Vasseghian, Y., Hojjati-Najafabadi, A., High-performance supercapacitors based on NiMn layered double hydroxides/Ni3S2 nanocomposite. *J Power Sources* **634**, 236465 (2025).

[15] Wang, R., Gao, J., Vijayalakshmi, M., Tang, H., Chen, K., Reddy, C.V., Kakarla, R.R., Anjana, P.M., Rezakazemi, M., Cheolho, B., Shim, J., Aminabhavi, T.M., Metal–organic frameworks and their composites: Design, synthesis, properties, and energy storage applications. *Chem Eng J* **496**, 154294 (2024).

[16] Bashir, T., Ghasali, E., Raza, S., Orooji, Y., Two-Dimensionally Aligned Vermiculite Nanoflakes with Built-In Diatomite Filler for Reversible Lithium-Ion Storage Performance. *J Nanostructure Chem* **15**, 152506 (2025).

[17] Wang, M., Guo, H., Xue, R., Li, Q., Liu, H., Wu, N., Yao, W., Yang, W., Covalent organic frameworks: A new class of porous organic frameworks for supercapacitor electrodes. *ChemElectroChem* **6**, 2984-2997 (2019).

[18] Sajjad, M., Lu, W., Covalent organic frameworks based nanomaterials: Design, synthesis, and current status for supercapacitor applications: A review. *J Energy Storage* **39**, 102618 (2021).

[19] Waller, PJ., Gándar, F., Yaghi, OM., Chemistry of covalent organic frameworks. *Acc Chem Res* **48**, 3053–3063 (2015).

[20] Hu, D., Jia, Y., Yang, S., Lin, C., Huang, F., Wu, R., Guo, S., Xie, K., Du, P., Hierarchical nanocomposites of redox covalent organic frameworks nanowires anchored on graphene sheets for super stability supercapacitor. *Chem Eng J* **488**, 151160 (2024).

[21] Li, R., Li, J., Liu, Q., Li, T., Lan, D., Ma, Y., Recent progress on covalent organic frameworks and their composites as electrode materials for supercapacitors. *Adv Compos Mater* **8** (2025) 86.

[22] Darabi, R., Karimi-Maleh, H., Zhong, N., Karimi-Harandi, M.H., Preparation of Fe-MOF/CuO/C3N4 as novel assemblies nanocomposites for high performance asymmetric supercapacitors. *Electrochim Acta* **480**, 143871 (2024).

[23] Yang, Y., Xu, D., Sun, Q., Li, Y., Zhang, W., Li, Z., Hu, Z., Anthraquinone-based covalent organic framework/reduced graphene oxide composites for supercapacitors. *J Energy Storage* **114**, 115881 (2025)

[24] Jameel, Y., Firdaus, A.H.M., Salit, M.S., Nanocomposites in energy conversion. *Phys Sci Rev* (2025) https://doi.org/10.1515/psr-2024-0028

[25] Wang, C., Zhou, E., He, W., Deng, X., Huang, J., Ding, M., Wei, X., Liu, X., Xu, X., $NiCo_2O_4$-Based Supercapacitor Nanomaterials, *Nanomaterials* **7**(2), 41 2017.

[26] Li, Y., Han, X., Yi, T., He, Y., Li, X., Review and prospect of $NiCo_2O_4$-based composite materials for supercapacitor electrodes.

J Energy Chem **31**, 54-78 (2019).

[27] Abouali, S., Garakani, MA., Xu, ZL., Kim, JK., $NiCo_2O_4$/CNT nanocomposites as bi-functional electrodes for Li ion batteries and supercapacitors. *Carbon* **102**, 262-272 (2016).

[28] Li, Q., Lu, C., Chen, C., Xie, L., Liu, Y., Li, Y., Kong, Q., Wang, H., Layered $NiCo_2O_4$/reduced graphene oxide composite as an advanced electrode for supercapacitor. *Energy Storage Mater* **8**, 59-67 (2017)

[29] Wu, P., Cheng, S., Yao, M., Yang, L., Zhu, Y., Liu, P., Xing, O., Zhou, J., Wang, M., Luo, H., Liu, M., A Low-Cost, Self-Standing $NiCo_2O_4$@CNT/CNT Multilayer Electrode for Flexible Asymmetric Solid-State Supercapacitors. *Adv Funct Mater* **27**, 1702160 (2017).

[30] Zhong, X., Shu, C., Su, X., Wang, W., Gong, J., Insight into improved oxygen evolution reaction on electronic modulation of phosphorus doped $NiCo_2O_4$. *Mater Today Commun* **31**, 103708 (2022).

[31] Zhang, H., Li, H., Wang, H., He, K., Wang, S., Tang, Y., Chen, J., $NiCo_2O_4$/N-doped graphene as an advanced electrocatalyst for oxygen reduction reaction. *J Power Sources* **280**, 640-648 (2015)

[32] Feng, X., Huang, Y., Li, C., Chen, X., Zhou, S., Gao, X., Chen, C., Controllable synthesis of porous $NiCo_2O_4$/NiO/Co_3O_4 nanoflowers for asymmetric all-solid-state supercapacitors. *Chem Eng J* **368**, 51-60 (2019).

[33] Wang, Z., Su, H., Liu, F., Chu, X., Yan, C., Gu, B., Huang, H., Yang, T., Chen, N., Han, Y., Establishing highly-efficient surface faradaic reaction in flower-like $NiCo_2O_4$ nano-/micro-structures for next-generation supercapacitors. *Electrochim Acta* **307**, 302-309 (2019).

[34] Choi, K., Moon, I.K., Oh, J., An efficient amplification strategy for N-doped NiCo 2 O 4 with oxygen vacancies and partial Ni/Co-nitrides as a dual-function electrode for both supercapatteries and hydrogen electrocatalysis. *J Mater Chem A* **7**, 1468-1478 (2019).

[35] Wang, Z., Li, H., Guo, Z., Liang, H., Jin, L., Li, M., Ao, Y., Porous Carbon Framework with B-Doped $NiCo_2O_4$ Nanoclusters for Enhancing the Performance of Carbon Fiber-Based Flexible Supercapacitors. *ACS Appl Nano Mater* **7**, 11816-11826 (2024).

[36] Yuvaraja, R., Sarathkumar, S., Gowsalya, V., Anitha Juliet, S.P., Veeralakshmi, S., Kalaiselvam, S., Hussain, S., Nehru, S., In situ synthesis of NiCo2O4/carbon nanocomposites: effect of carbon content and symmetric/asymmetric device configuration on supercapacitor performance. *New J Chem* **48**, 15556-15566 (2024).

[37] Zhou, Y., Li, C., Li, X., Huo, P., Wang, H., Construction of high-performance electrode materials of $NiCo_2O_4$ nanoparticles encapsulated in ultrathin N-doped carbon nanosheets for supercapacitors. *Dalton Trans* **50**, (2021) 1097-1105

[38] Mulik, S.V., Koyale, P.A., Soni, S.S., Maske, S.M., Dongale, T.D., Sutar, S.S., Parale, V.G., Park, H.H., Delekar, S.D., Optimized Fabrication of Supercapacitor Using MOF-Derived $NiCo_2O_4$ with Porous Carbon as Cathode: Electrochemical Characterization and Stability Analysis using Time Series Analysis Technique. *ACS Appl Electron* **6**, 4369-4380 (2024).

[39] Bhatti, M.A., Kumar, S., Tahira, A., Bhatti, A.L., Ujjan, Z.A., Jakhrani, M.A., Aftab, U., Alshammari, R.H., Nafady, A., Dawi, E., Emo, M., Vigolo, B., Infantes-Molina, A., Ibupoto, Z.H., Advanced $NiCo_2O_4$/ZnO-CuO/NF composite for high-performance asymmetric supercapacitor and efficient oxygen evolution reaction applications, *Adv Compos Hybrid Mat* **8**, 148 (2025).

[40] Chen, S., Gao, P., Zhang, D., Lin, L., Huang, L., Li, Z., Lan, Z., Jiang, Y., Ru, Q., Zhou, G., Liu, J.M., Kempa, K., Gao,V., Flexible asymmetric supercapacitors based on $NiCo_2O_4$ in a neutral electrolyte achieving 2.4 V voltage window. *J Alloys Compd* **860**, 158346 (2021).

[41] Wang, W., Qi, J., Sui, Y., He, Y., Meng, Q., Wei, F., Jin, Y., An Asymmetric Supercapacitor Based on Activated Porous Carbon Derived from Walnut Shells and $NiCo_2O_4$ Nanoneedle Arrays Electrodes, *J Nanosci Nanotechnol* **18**, 5600-5608 (2018).

Supporting Information

Table S1. Performance metrics of NF/ COF/$NiCo_2O_4$-N-doped//AC/NF ASC cell

Sample ID	Current Density ($A.g^{-1}$)	Specific Capacitance ($F. g^{-1}$)	E ($W.h.kg^{-1}$)	P ($W. kg^{-1}$)
NF/ COF/$NiCo_2O_4$-N-doped//AC/NF	2	172.96	34.59	1235.75
	3	31.8	31.8	1870.58
	4	146.66	29.33	2444.16
	5	137.0	27.4	3044.44
	6	110.0	22.0	3666.66
	7	108.83	21.76	4352.0
	8	73.33	14.66	4886.6

10.57647/jnsc.2026.1602.09